

## Article

# Analysis of Inner Flow in a Multi-Stage Double-Suction Centrifugal Pump Using the Detached Eddy Simulation Method

Wenjie Peng <sup>1</sup>, Ji Pei <sup>1,\*</sup> , Shouqi Yuan <sup>1</sup>, Jiabin Wang <sup>2</sup>, Benying Zhang <sup>2</sup>, Wenjie Wang <sup>1,3,4,\*</sup>  and Jiaxing Lu <sup>4</sup><sup>1</sup> National Research Center of Pumps, Jiangsu University, 301 Xuefu Road, Zhenjiang 212013, China<sup>2</sup> Shandong Shuanglun Co., Ltd., Weihai 264203, China<sup>3</sup> Wenling Research Institute of Fluid Machinery, Jiangsu University, Taizhou 317522, China<sup>4</sup> Key Laboratory of Fluid and Power Machinery, Xihua University, Chengdu 610039, China

\* Correspondence: jpei@ujs.edu.cn (J.P.); wenjiewang@ujs.edu.cn (W.W.)

**Abstract:** In order to analyze the inner flow in a multi-stage double-suction centrifugal pump, which is regarded as a common way of knowing the current characteristics of the pump and as the basis of optimization for better performance, a numerical simulation considering the velocity field distribution characteristics and pressure fluctuation propagation law using the detached eddy simulation method was conducted. Additionally, the principle of entropy generation was put to use to quantify and compare the energy loss of different components. The results reveal that the existence of unstable flow structures in the first-stage impeller and a large number of vortical structures in the back-channel result in reduced operational efficiency of the pump. Furthermore, the pressure fluctuation intensity reaches its maximum with 0.15 at the blade trailing edge, which propagates to the tongue region of the forward flow channel and the double-volute under the low rates condition. Additionally, the main frequency of the monitoring points in the inter-stage flow channel and volute is basically located at a frequency of 198.667 Hz, which is twice the blade frequency. Consequently, the wall entropy production accounting for nearly 25% cannot be ignored and that the loss mainly occurs in the double-volute and the inter-stage flow channel due to the occurrence of irregular flow in the above components with more than 50%. The outcomes of this research present a valuable point of reference for the optimization of structural design in multistage turbomachines with various applications.

**Keywords:** multi-stage double-suction centrifugal pump; detached eddy simulation; vortex



**Citation:** Peng, W.; Pei, J.; Yuan, S.; Wang, J.; Zhang, B.; Wang, W.; Lu, J. Analysis of Inner Flow in a Multi-Stage Double-Suction Centrifugal Pump Using the Detached Eddy Simulation Method. *Processes* **2023**, *11*, 1026. <https://doi.org/10.3390/pr11041026>

Academic Editor: Federica Raganati

Received: 6 March 2023

Revised: 24 March 2023

Accepted: 25 March 2023

Published: 28 March 2023



**Copyright:** © 2023 by the authors. Licensee MDPI, Basel, Switzerland. This article is an open access article distributed under the terms and conditions of the Creative Commons Attribution (CC BY) license (<https://creativecommons.org/licenses/by/4.0/>).

## 1. Introduction

The multi-stage double-suction centrifugal pump is a centrifugal pump with an inlet on both sides and an outlet in the middle. In addition, the combination of multiple single-suction impellers and one double-suction impeller, which uses the same impeller hydraulic models, is adopted. Compared with the traditional centrifugal pumps, it not only has the advantages of a large volume of flow but also has the ability of a higher head due to the multi-stage structure [1]. Meanwhile, a double volute design could be well achieved to reduce the influence of radial force. At present, multi-stage double-suction pumps are widely applied in the continuous transportation of water, especially in long-distance water diversion projects and agricultural irrigation pumping stations. Therefore, it has great application prospects. However, due to their unique structure, multi-stage double-suction pumps are prone to generate flow losses, especially in the inter-stage flow channel, which is related to the occurrence of vortices and leads to the degradation of pump performance. [2,3].

Nowadays, there is a variety of literature related to the flow characteristics of centrifugal pumps that captures the phenomenon of disturbed normal flow and explores the

source of flow instability. Among them, the components of the double-suction centrifugal pumps would be one of these factors. Xia et al. [4] used the particular algorithm to study the special phenomena, which focused on tip clearance and captured leakage flow and secondary backflow in certain regions. Different from the former, Chung et al. [5] investigated the other components, which include the impeller and volute, to quantify the interaction between them, which influences the intense fluctuation of pressure. It is noteworthy that the interaction is commonly found in centrifugal pumps, which results in unstable flow and noise. González et al. [6] carried out the rotor-stator interaction on the pump shaft to calculate the radial forces. Baun et al. [7] developed a new technology to measure the radial impeller forces, which also result from the interaction between the impeller and collector housing. Similarly, Barrio et al. [8] investigated the flow pulsations, which were also related to the effect between the blades and tongue based on a validated model. Choi et al. [9] measured the velocity and pressure data of the impeller to investigate the law of flow process and further explore the source of noise. Different from the former, Kelder et al. [10] set up different locations on the volute rather than the impeller to study the velocity field and static pressure. Although the flow deviations were found, they would not affect the performance of the pump significantly.

Generally, the literature on turbulence models mainly focuses on the Reynolds-Averaged Navier–Stokes Simulation (RANS) and the Large Eddy Simulation (LES). However, the selection of the previously mentioned turbulence model [11] would not be applicable to all situations, which affects the accuracy of the results. Thus, a compromise approach should be considered to address the dilemma. In 1997, the Detached Eddy Simulation of the model was first proposed by Spalart [12], which took into account the advantages of the RANS method and LES method and had the characteristics of a simple structure and easy application. Therefore, the DES method has been applied to the internal flow field analysis of fluid machinery by more and more scholars at home and abroad. Zhu et al. [13] investigated the flow field based on the DES model to identify the source of unstable head variation and improved it by adjusting the guide vane opening. Minakov et al. [14] adopted the DES model and the Reynolds stress equation model (RSM) simultaneously to analyze the flow in a draft tube and summarized that the calculated results of the DES model are more consistent with the experimental data. Tao et al. [15] studied the internal flow characteristics of the reactor coolant pump via the DES model and accurately predicted head and efficiency. Yang et al. [16] adopted the DES model to study the radial rotating characteristics before the existence of rotating stall, analyzing the reasons for the phenomenon at the same time. Wu et al. [17] applied the DES method to examine and certify the PIV test results.

In summary, although the DES method obtains more and more attention in fluid machinery, with a large number of papers published, most of these studies generally focus on models with a relatively simple structure. At the same time, ensuring the convergence and accuracy of the calculation is also complicated. As a result, there is little research on this aspect. In this paper, the unsteady flow characteristics of a multi-stage double-suction centrifugal pump are studied based on the DES method. Moreover, the mechanisms of the phenomenon are explained. In Section 2, the three-dimensional model and computational grid are shown, which are the basics of the simulation. Then, in Section 3, the turbulence model, boundary conditions for numerical simulation, and validation of numerical simulation are described, which provides the necessary steps for accurate simulation. Subsequently, in Section 4, the change of flow field is explored, and the energy loss distribution law is analyzed with the entropy generation theory. Finally, the conclusion is given in Section 5.

## 2. Numerical Model and Computational Domain

### 2.1. Three-Dimensional Model and Design Parameters

The studied pump is manufactured according to the requirements of the design condition, where the rotating speed is set at 1490 rpm. The design flow rate and head are set at 0.15 m<sup>3</sup>/h and 132 m, respectively, to meet the demand of water carrying and lifting.

The realistic picture and computational model of the researched pump are listed in Figure 1a,b. From the picture, the components of the pump are shown separately, including five main parts. It should be noted that the same impeller hydraulic models are applied to both different impellers. And the double-volute inter-stage flow channel is composed of a positive flow passage, a bridge section, and a reverse flow passage. At the same time, the length of the inlet connected with the suction chamber and the outlet in junction with the double volute are extended by 8 times the diameter of the pipeline to reduce the influence of the reverse flow vortex.

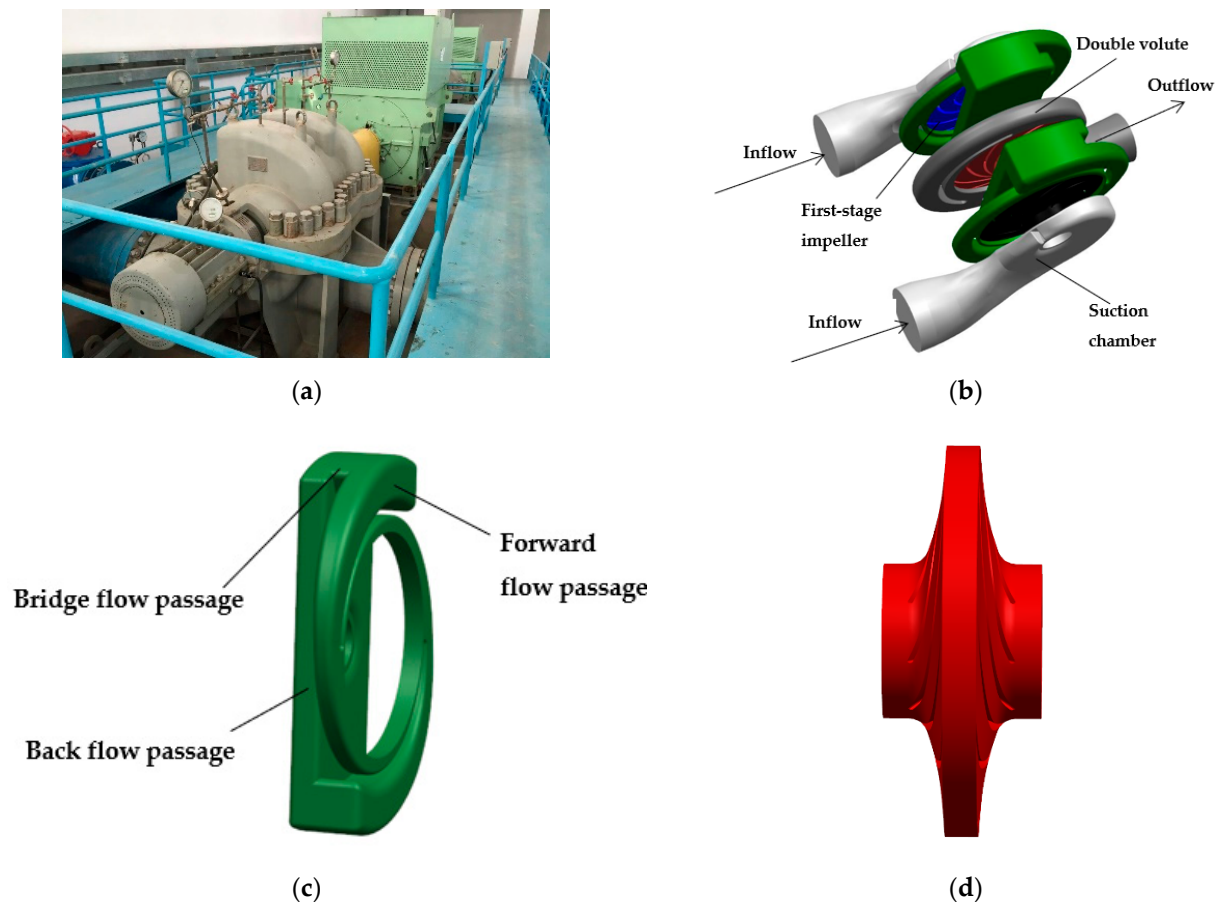


**Figure 1.** Three-dimensional model of the pump, which includes (a) Physical drawing, (b) assembly drawing, (c) inter-stage flow channel, and (d) second-stage impeller.

## 2.2. Computational Grid and Grid Convergence Analysis

Grid is the basis of discretization of control equation space and the key part of numerical simulation pretreatment, which is mainly divided into unstructured grid, mixed grid, and structured grid. Due to the complexity of the overall three-dimensional structure, it is necessary to generate a suitable grid, considering the mesh quality and calculation time. Because of their advantages in computing resources and convergence, structured grids are widely used in pump analysis. Furthermore, the quality of the grid can determine the computational accuracy and efficiency of fluid dynamics.

The grids of the model were structurally divided into hexahedrons of rotating and stationary domains using Turbo Grid and ANSYS ICEM, and H/O topology was adopted at the impeller. As a result, the grid quality value is above 0.3 and the angle of the mesh is beyond  $14^\circ$ .

The height of the first layer of grid at the critical wall of each component is less than 0.1 mm, and the growth rate of grid height is between 1.15 and 1.3. The details of structured mesh are shown in Figure 2.

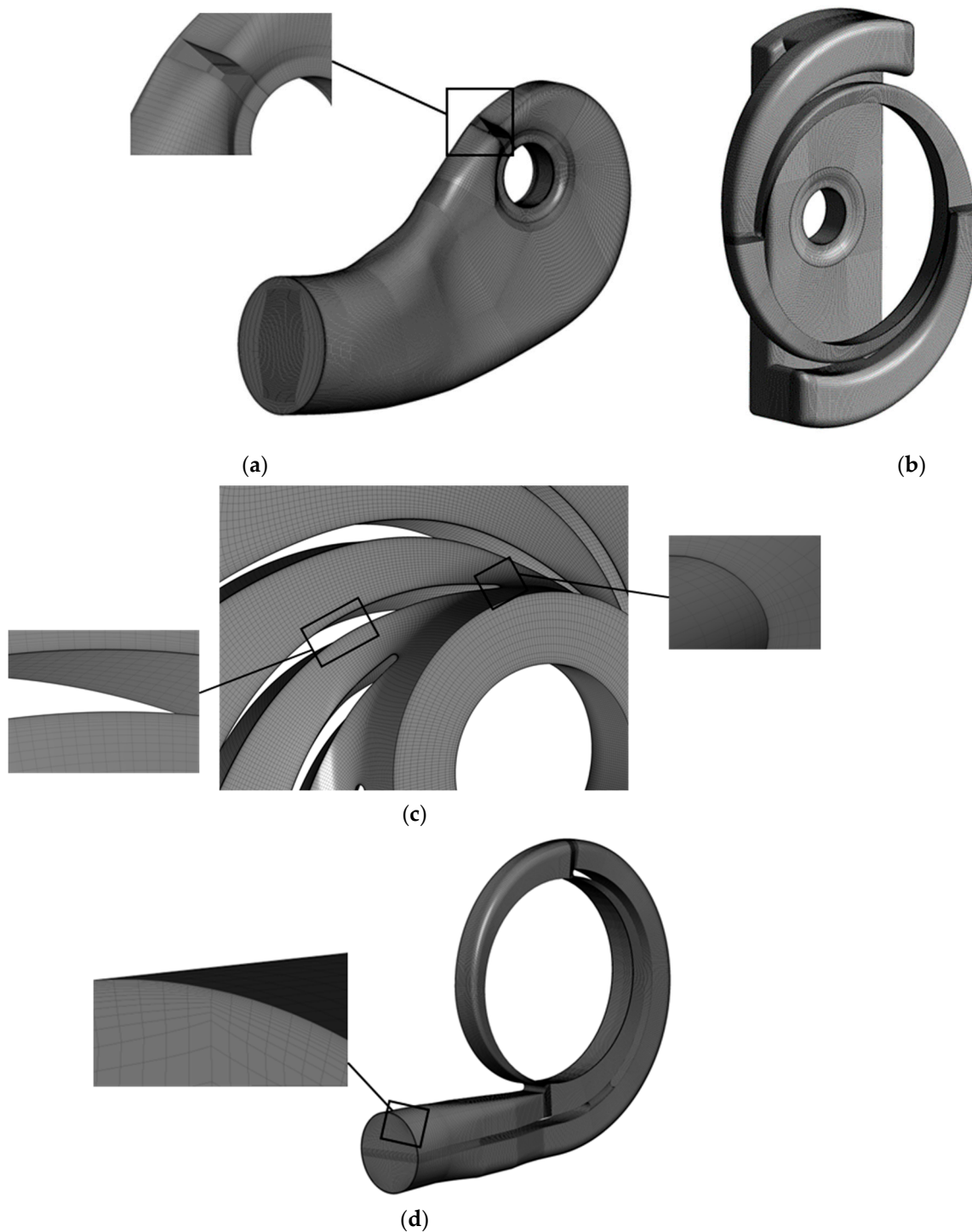


**Figure 2.** Structured mesh of all domains, which includes (a) suction chamber, (b) inter-stage flow channel, (c) impeller, and (d) double volute.

To meet the high requirements of the SST  $k-\omega$  turbulence model, the wall surface value  $y^+$  was considered to achieve the accuracy of results and the distribution of  $y^+$  value on the blade wall surface, with the maximum value less than 1. The average  $y^+$  value of each component is calculated, and the maximum value is less than 40. The result of the near-wall grid size fully meets the requirements of the DES turbulence model in the reference paper [18].

The grid convergence index (GCI) criterion is adopted for grid convergence analysis. Accordingly, three different grid systems with mesh numbers of 29.43, 12.85, and 5.67 million were generated, and a grid refinement factor exceeding 1.3 was achieved. Furthermore, the dimensionless variable  $w_r/u$  was selected as an important indicator for grid convergence. The locations of the points on the impeller were labeled and ranged from the pressure side to the suction side, corresponding to  $0^\circ$  to  $45^\circ$ . The GCI value corresponding to each key variable was calculated and the maximum value is 4.02%, which is lower than the recommended value of 5%. Additionally, the comparison between the values of key variables corresponding to the fine-grid scheme and the extrapolated values shows that the two curves are almost identical.

Considering the results, the fine-grid scheme is chosen to capture small-scale vortices as much as possible and further explore the vortex characteristics. In addition, the specific grid numbers of the fine-grid scheme on the suction pipe, suction chamber, first-stage impeller, inter-stage flow channel, second-stage impeller, double volute, and discharge pipe are 745,000, 2,848,000, 3,163,000, 2,792,000, 6,809,000, 2,869,000, and 655,000, respectively.

### 3. Numerical Methodology

#### 3.1. Turbulence Model

The flow in a centrifugal pump, regardless of the flow rate, is governed by the law of conservation, in physics. The corresponding control methods include the continuity equation, the momentum equation, and the energy equation. In addition, the energy equation should not be considered because energy transfer does not occur when the centrifugal pump is running. For all of these present simulations, the flow is assumed to be a three-dimensional viscous, incompressible, and unsteady flow.

- (1) The continuity equation, according to the continuity hypothesis of fluid, is expressed by the differential equation as follows:

$$\frac{\partial \rho}{\partial t} + \frac{\partial(\rho u_i)}{\partial x_i} = 0 \quad (1)$$

where  $\rho$  is the density of the fluid,  $u_i$  denotes the fluid velocity component in the coordinate  $x_i$  direction, and  $t$  stands for the time.

- (2) The momentum equation is as follows:

$$\frac{\partial(\rho u_i)}{\partial t} + \frac{\partial(\rho u_i u_j)}{\partial x_j} = -\frac{\partial p}{\partial x_i} + \frac{\partial \tau_{ij}}{\partial x_j} + S_{mi} \quad (2)$$

where  $P$  stands for the static pressure;  $S_{mi}$  is the generalized source term of the momentum equation, including gravity, and the force between multiphase flow, etc. Where  $\tau_{ij}$  belongs to the Reynolds stress terms.

The Detached Eddy Simulation (DES) is a typical RANS/LES (Reynolds Time-Average Simulation and Large Eddy Simulation) hybrid method, which is specially used for unsteady flow analysis [12]. The DES method filters the solution region through grid scale and uses different turbulence models in different regions. The DES method used in this study is based on the SST  $k$ - $\omega$  model [19]. The  $K$  equation and  $\omega$  equation are as follows:

$$\frac{\partial(\rho k)}{\partial t} + \frac{\partial(\rho k u_i)}{\partial x_i} = P_k - \frac{\rho k^{3/2}}{l_{RANS}} + \frac{\partial}{\partial x_j} \left[ \left( \mu_t + \frac{\mu_t}{\sigma_k} \right) \frac{\partial k}{\partial x_j} \right] \quad (3)$$

$$\frac{\partial(\rho \omega)}{\partial t} + \frac{\partial(\rho \omega u_i)}{\partial x_i} = C_\omega P_\omega - \beta_\omega \rho \omega^2 + \frac{\partial}{\partial x_j} \left[ \left( \mu_t + \frac{\mu_t}{\sigma_k} \right) \frac{\partial \omega}{\partial x_j} \right] + 2\rho(1 - F_1) \frac{1}{\sigma_{\omega 2}} \frac{1}{\omega} \frac{\partial k}{\partial x_i} \frac{\partial \omega}{\partial x_i} \quad (4)$$

where the dimensionless eddy viscosity coefficient  $\mu_t$  is as follows:

$$\mu_t = \min \left[ \frac{\rho k}{\omega}, \frac{a_1 \rho k}{\Omega F_2} \right] \quad (5)$$

$P_k$  and  $P_\omega$  are the turbulence generation terms. Both  $F_1$  and  $F_2$  are mixed functions. The turbulent length dimension  $l_{\text{RANS}}$  is defined as follows:

$$l_{\text{RANS}} = \frac{k^{1/2}}{\beta_k \omega} \quad (6)$$

In the DES method, the turbulence length dimension  $l_{\text{RANS}}$  is replaced by the DES length dimension  $l_{\text{DES}}$ .

$$l_{\text{DES}} = \min(l_{\text{RANS}}, l_{\text{LES}}) \quad (7)$$

$$l_{\text{LES}} = C_{\text{DES}} \Delta \quad (8)$$

$$\Delta = \max\{\Delta x, \Delta y, \Delta z\} \quad (9)$$

$l_{\text{LES}}$  is the filtering size of the LES sub-lattice model;  $\Delta$  is the maximum grid scale of the cell in three directions; and  $C_{\text{DES}}$  is the model coefficient.

In the near-wall region,  $l_{\text{DES}} = l_{\text{RANS}}$ , the dissipation term  $k$  is the same as that of conventional RANS, which means DES is solved by the RANS model. On the other hand, if  $l_{\text{DES}} = l_{\text{LES}}$ , the dissipative term of the transport equation is defined as  $\frac{\rho k^{3/2}}{C_{\text{DES}} \Delta}$ , which means DES is solved by the LES model [20,21].

### 3.2. Boundary Conditions

In this paper, the steady-state results calculated by the SST  $k$ - $\omega$  (Shear Stress Transport) turbulence model are used as the initial conditions for the subsequent unsteady calculation, which utilizes the DES turbulence model through ANSYS CFX. The discrete method employed in the steady calculation is the first-order upwind scheme to meet the requirement of convergence.

The boundary conditions settings are divided into two parts, with total pressure inlet and mass flow outlet set for unsteady calculation. Wall conditions are set to non-slip, which means the default wall velocity is 0. The near-wall function was processed with the standard wall function embedded in CFX. At the same time, with reference to the articles on the effect of wall roughness and in combination with the actual situation of the test pump, the equivalent wall roughness was finally set to 20  $\mu\text{m}$ . For better convergence, the second-order upwind scheme was selected instead of the central difference scheme. Convergence residuals were set to  $10^{-5}$  and the transient time step was set to 0.00033557 s, which was equal to an angle of 3 degrees of rotation of the impeller. The total time was input at 0.604027 s, with the aim of studying the internal flow change of the impeller after 15 revolutions.

Meanwhile, during the period of calculation, several physical quantities are monitored, and the calculation is considered the beginning of convergence when it presents stable periodic fluctuations. Finally, as the difference between the mass flow rates at the inlet and outlet is less than 0.1%, the result is in a stable state.

### 3.3. Validation of Numerical Simulation

This test includes the calculation of the external characteristics of the pump, which is an inevitable step in verifying the simulation. After adjusting the outlet valve to change the flow, the head and efficiency of the test pump were obtained through testing when stabilized. The corresponding numerical simulation results are based on the average of the results of the last five cycles of unsteady calculation. Since the simulated efficiency

does not include volume loss and mechanical loss, the empirical formula of the loss calculation is adopted to estimate the total efficiency of the pump. Then these parameters are dimensionless to obtain the head coefficient  $\Psi$ .

$$\Psi = \frac{gH}{u^2} \quad (10)$$

where  $u$  denotes the circumferential velocity at the impeller outlet.

From Figure 3, the head coefficient of the simulation decreases at a slow speed with flow increase, which is close to the result on the test rig. However, there is a certain difference between the two kinds of results that is especially larger under extreme conditions. Additionally, the phenomenon that the result of the simulation almost outweighs the test value except under design conditions may come from the loss in the field pipeline and other flow instability without consideration. However, the efficiency of simulation goes through a process of rising first and reaches the highest point of 75.9% under the design flow, then it declines. And the result of the simulation is also greater than the result of the experiment. Specifically, at the design operating point, the proportional error between the simulated efficiency and the experimental value is 2.4%, while the deviation in the head coefficient is 1.8%. Totally, two pairs of data are almost consistent with each other.

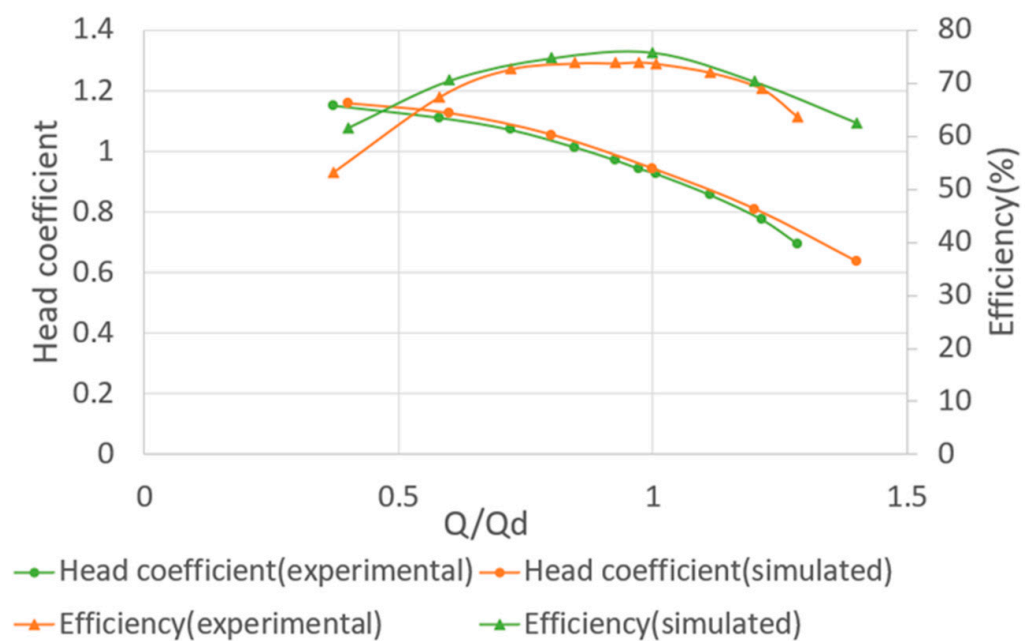


**Figure 3.** Performance comparison between numerical and experimental results.

## 4. Results and Discussion

### 4.1. Velocity Distribution

Figure 4 shows the velocity distribution on the mid-section of the suction chamber at different flow rates. The inner flow in the suction chamber is relatively uniform, and the velocity shows an upward trend from the inlet to the outlet, finally reaching the maximum near the outlet. Consequently, a high-speed zone similar to a ring is generated near the exit. Meanwhile, due to the rib structure, vortices of different scales are generated nearby as a result of high circumferential speed.

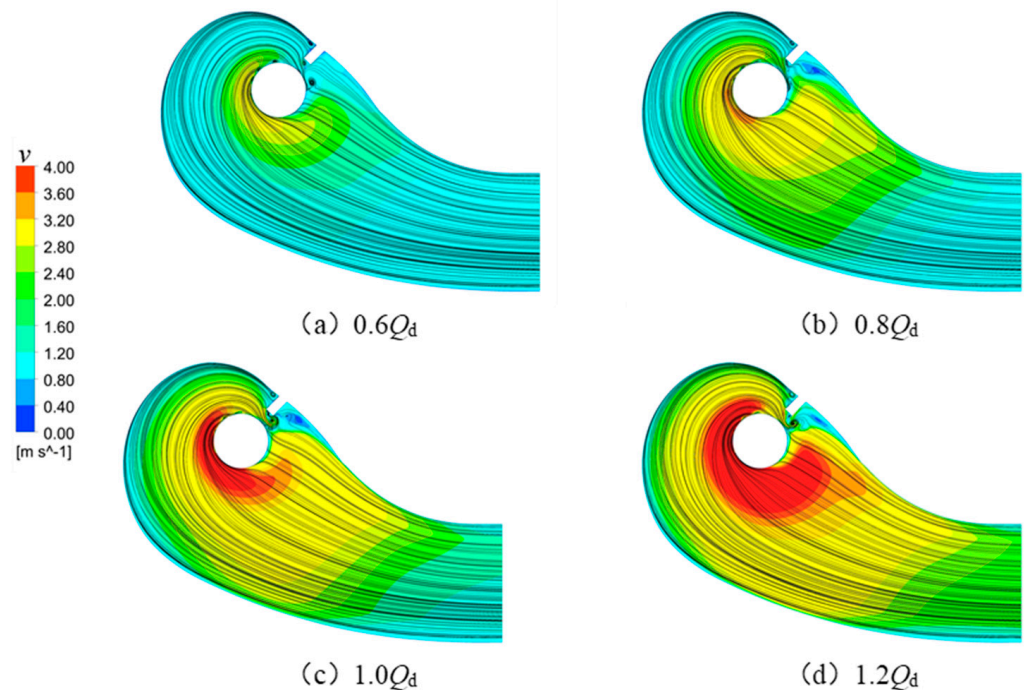


**Figure 4.** Velocity distribution in the suction under different flow rates.

From Figure 4a–d, the range of the high-speed flow area of the fluid gradually expands circularly. Furthermore, the closer to the exit, the higher the speed. Whether under the eccentric condition or under the design condition, there always exists a certain number of small-scale eddies near the outlet because of the back-flow. This phenomenon is particularly obvious under low flow conditions due to the increment of reflux, intensifying the blockage in the flow passage of the first-stage impeller.

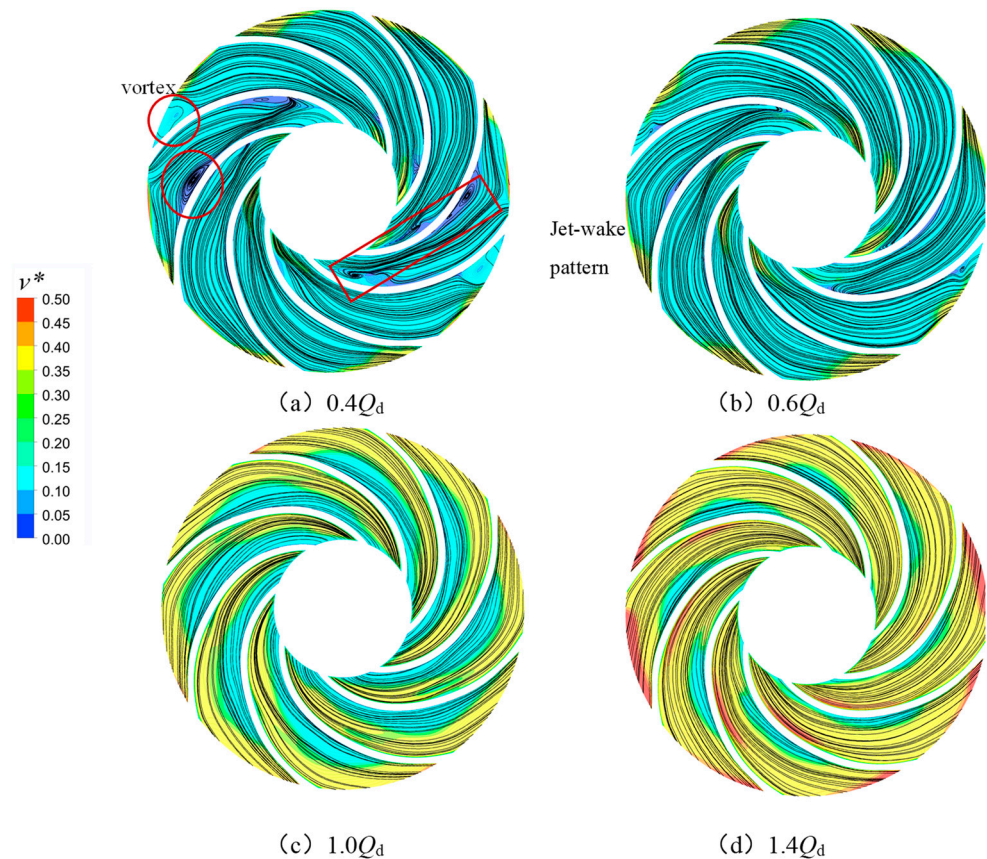
Under the condition of deviating from the design flow, some unstable flow phenomena in the impeller of a centrifugal pump, such as flow separation and jet wake, are clear. Figure 5 presents the relative velocity distribution on the mid-span of the first-stage impeller under different flow rates. For better analyzing the velocity field distribution characteristics of the first-stage impeller, the velocity coefficient  $v^*$  is introduced  $v^*$ , which is shown as follows:

$$v^* = \frac{v}{u} \quad (11)$$

where  $v$  is the relative velocity (m/s) and  $u$  is the outlet circumferential speed of the first-stage impeller (m/s).

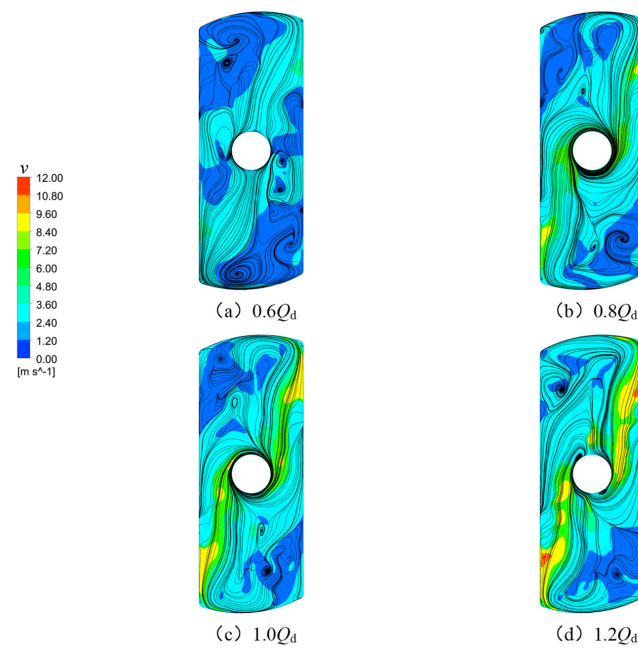
Figure 5 shows that the relative velocity distribution in the first-stage impeller shows certain symmetrical distribution characteristics under the given conditions. Four conditions different from those on other components, ranging from  $0.4 Q_d$  to  $1.4 Q_d$ , are selected to investigate the first-stage impeller due to the obvious phenomena, such as a large-scale vortex at  $0.4 Q_d$  and a high-speed zone at  $1.4 Q_d$ , which have a great impact on the efficiency of the pump. In total, the pressure side velocity is less than the suction side velocity, especially under the large flow condition of  $1.4 Q_d$ . Figure 5d shows that the low-speed zone covers nearly half of the length of the blade pressure side, resulting in flow separation. As the flow decreases to  $0.6 Q_d$ , the low-speed zone almost expands to the whole impeller channel. In addition, small-scale vortices begin to appear in impeller channels at random. The velocity changes suddenly near the pressure side, which forms an unstable flow structure comparable to a jet wake, as shown in red square. Furthermore, flow separation becomes more serious when the flow is reduced to the minimum working condition, which evolves into large-scale vortex structures near the impeller outlet, as shown in the red circles. In a word, the phenomenon mentioned above is the reason

why efficiency decreases rapidly at low flow rates. In order to solve the above problems, multi-objective optimization is considered to achieve efficient operation of the modified pump under low flow conditions. Considering that optimizing individual components has certain limitations on improving pump performance, matching optimization of the impeller and other stationary components can also be considered to ultimately improve the efficiency of this type of pump.



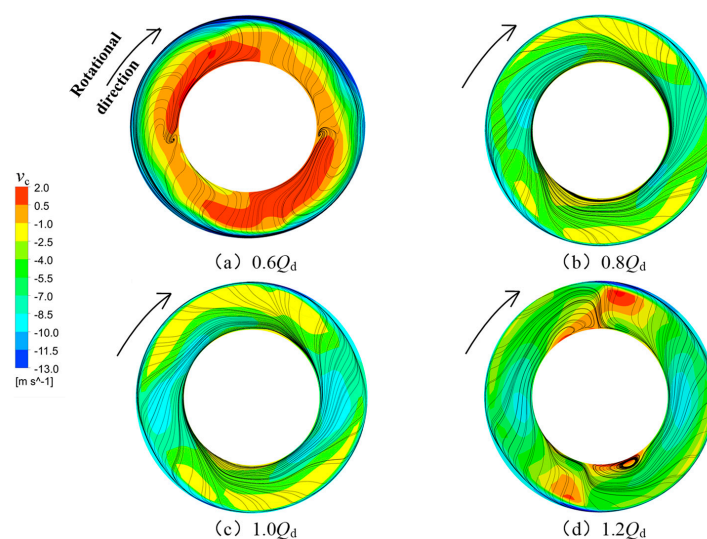
**Figure 5.** Relative velocity distribution on the mid-span of the first-stage impeller under different flow rates.

Figure 6 shows the velocity distribution on the mid-span of the back channel, which is a part of the inter-stage flow channel, under different flow rates. As a whole, the flow phenomenon in the back channel is similar under different conditions. After passing through the bridge channel, the fluid still maintains a certain speed and enters the reverse flow channel, finally entering the second-stage impeller through a pressure difference. Moreover, due to the symmetrical structure, the internal velocity distribution also has a certain symmetry, especially in the vicinity of the outlet and the wall near the bridge channel. The vortex structure exists, which has a negative impact on the internal flow pattern of the reverse flow channel due to the lack of a splitter. Therefore, this structure makes it easy to have a large rotation speed when the fluid flows into the second-stage impeller, which produces unnecessary energy consumption, influencing the operation stability and reducing the pump's performance. Meanwhile, in subsequent studies, unstable flow was controlled by adding baffles. According to previous research [19], we found that these scholars have achieved efficiency improvements by adding a baffle structure but have not analyzed the impact of the baffle position and shape on efficiency. Therefore, in subsequent research, parametric modeling of the baffle studies the impact of this structure on the overall performance of multi-stage double-suction centrifugal pumps.



**Figure 6.** Velocity distribution on the mid-span of the back channel under different flow rates.

The research of relevant scholars shows that the inlet pre-whirl has a great impact on the instability of the fluid machinery. Figure 7 shows the pre-whirl distribution at the inlet of the second-stage impeller in order to analyze the inflow state. Figure 7 shows that under the four typical working conditions, the circumferential velocity near the hub is almost negative, and under the working conditions of  $0.6 Q_d$  and  $1.2 Q_d$ , there is an obvious vortex structure near the hub, indicating that the flow here is irregular. The average pre-whirl velocities corresponding to the four different conditions are  $-3.28$  m/s,  $-4.99$  m/s,  $-5.36$  m/s and  $-15.84$  m/s, respectively, which suggests that as the flow increases, the absolute value of the circumferential velocity at the inlet of the second-stage impeller also increases, and the influence of pre-whirl on the head of the second-stage impeller will also be greater. Overall, the inter-stage flow channel worsens the inflow conditions at the inlet of the second-stage impeller, leading to a large number of unstable structures in the pump, affecting the efficiency and stable operation of the pump.



**Figure 7.** Circumferential velocity distribution of the inlet for the second-stage impeller under different flow rates.

Figure 8 shows the velocity distribution of the second-stage impeller and volute under different flow rates. Overall, the tendency of the velocity distribution in the above two computational domains are relatively consistent with each other. The flow process shows that the fluid first enters the second-stage impeller at a low speed, and then the energy is obtained through the rotation. In addition, the impeller here has similar characteristics with the first-stage impeller, producing the low-speed zone. After the fluid enters the volute, the fluid's energy source switches from kinetic energy to pressure energy, resulting in the lowest speed at the discharge outlet.

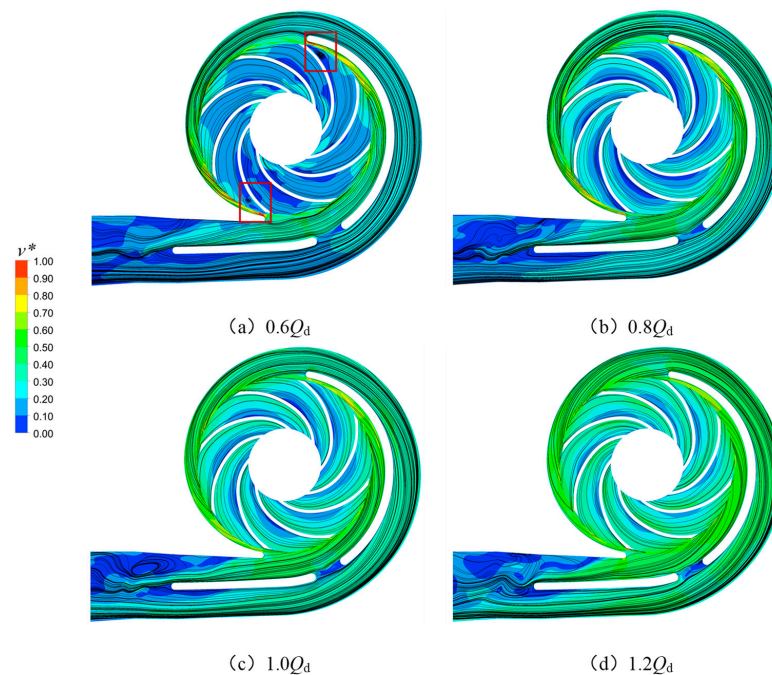


**Figure 8.** Velocity distribution of the second-stage impeller and volute under different flow rates.

According to the previous analysis, the fluid flowing into the second-stage impeller has a very high pre-whirl speed, which also leads to the uneven velocity streamline in the impeller channel and the flow separation phenomenon. In Figure 8a, the intensification of the rotor-stator interaction leads to the generation of a high-speed flow area near the initial position of the splitter and the tongue of the volute. The distribution of the impeller outlet streamline near the above two positions is also very disordered, and the wake vortex is even clearly seen under  $0.6 Q_d$  conditions (as shown in the red squares), which undoubtedly cause great energy loss. However, the blockage in the second-stage impeller channel is alleviated along with the increased flow, and the streamline gradually becomes smooth. Overall, providing the original double-volute design is not reasonable. Consideration is given to subsequent improvements in the placement of the separator and the cross-sectional shape of the volute.

#### 4.2. Pressure Fluctuation Characteristics

For studying the law of pressure fluctuation change of the model pump in the unsteady process and exploring the characteristic frequency and excitation source of various complex pressure fluctuations, this section selects the data of the last 8 cycles of the DES turbulence model calculation results for each typical working condition through the use of the pressure fluctuation intensity coefficient and the Fast Fourier transform method.

In the process of unsteady simulation, the pressure solution result  $p$  of each grid node is the periodic result of a phase average, which is composed of two parts: the time-averaged pressure component  $\bar{p}$  and the periodic pressure component  $\tilde{p}$ , where the periodic

pressure component  $\tilde{p}$  is generated by the periodic change in blade passage frequency. The expression of the two components is as follows:

$$\bar{p}(\text{node}) = \frac{1}{N} \sum_{j=0}^{N-1} P(\text{node}, t_0 + j\Delta t) \quad (12)$$

$$\tilde{p}(\text{node}, t) = p(\text{node}, t) - \bar{p}(\text{node}) \quad (13)$$

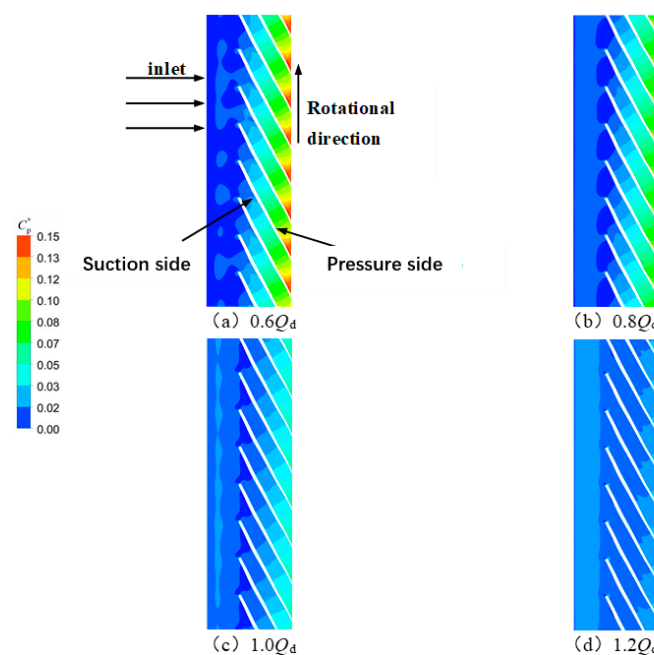
where *node* represents the grid node; *N* is the sampling number of pressure *p* when the impeller rotates one circle; *t*<sub>0</sub> represents the initial time (s); *j* is the number of time steps.

This paper introduces the pressure fluctuation intensity coefficient  $C_p^*$  to obtain the pressure fluctuation intensity change rule of a research pump in one impeller rotation cycle. Its specific expression is shown in the following equation:

$$C_p^* = \frac{\sqrt{\frac{1}{N} \sum_{j=0}^{N-1} \tilde{p}(\text{node}, t_0 + j\Delta t)^2}}{\frac{1}{2}\rho u^2} \quad (14)$$

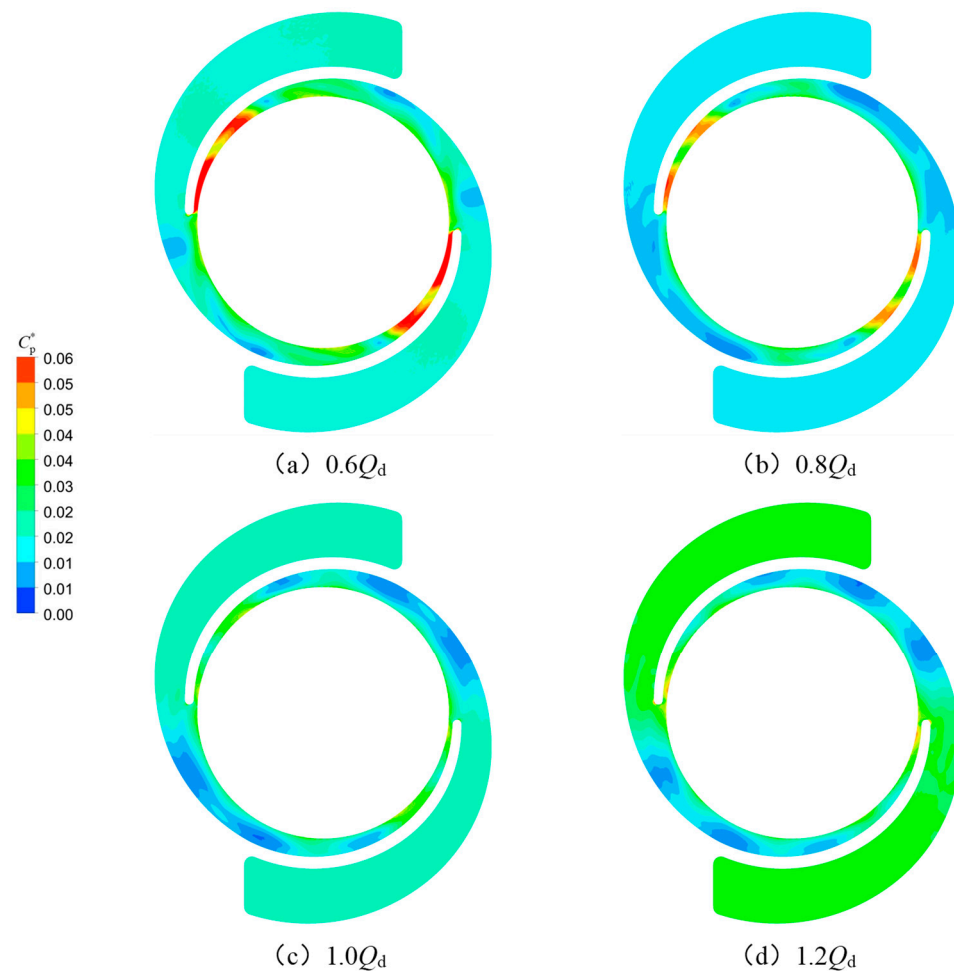
where *u* is the circumferential speed of the impeller outlet. From the formula, the essence of  $C_p^*$  is to obtain the dimensionless result of the pressure standard deviation of each node in a rotation cycle. Therefore,  $C_p^*$  is positively correlated with pressure fluctuation and pressure fluctuation intensity and reflects the overall pressure fluctuation intensity in a rotating cycle.

Figure 9 shows the blade-to-blade view of pressure fluctuation intensity of the first-stage impeller under different working conditions when the blade height is 0.5 (the blade height is 0 for the hub and the blade height is 1 for the shroud). The impeller inlet direction and other information are detailed in Figure 9a. Evidently, the pressure fluctuation intensity on the pressure side of the blade reaches its maximum at blade trailing edge. Under conditions from 0.6  $Q_d$  to 1.2  $Q_d$ , the intensity in the impeller channel decreases gradually, but shows an upward trend near the inlet of the impeller. The main reason for this is because the energy exchange at the interface and the suction chamber becomes more intense under the increased flow rate.



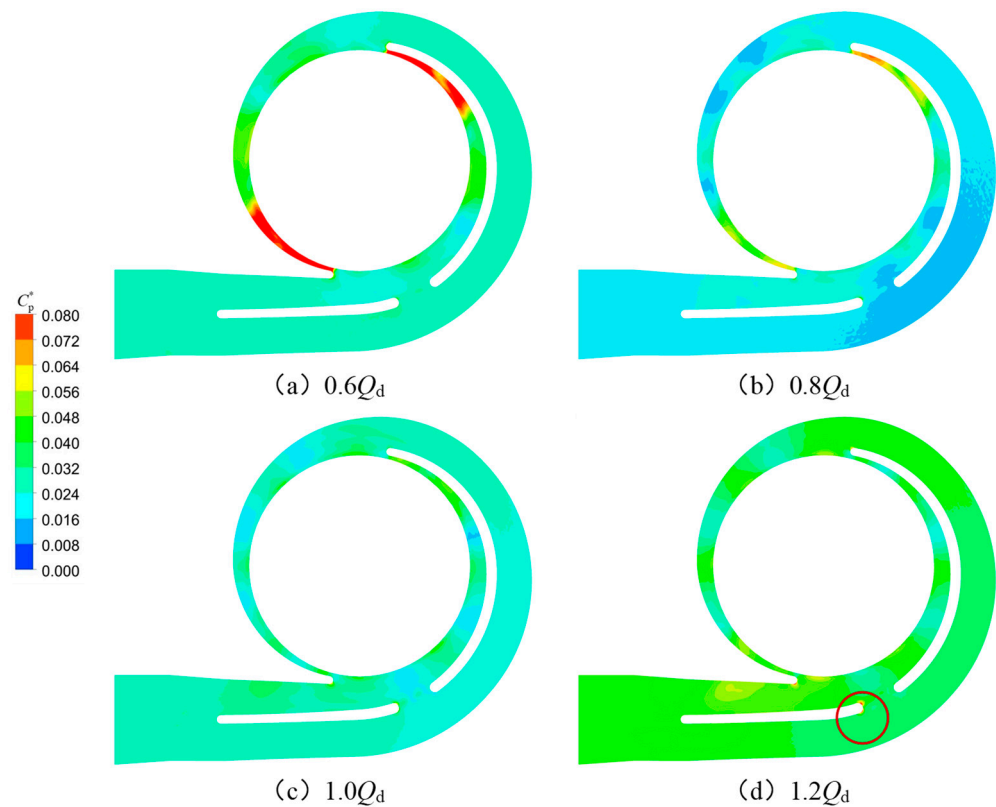
**Figure 9.** Blade to blade view of the pressure fluctuation intensity distribution of the first-stage impeller under different flow rates.

Figure 10 displays the pressure fluctuation intensity distribution in the axial section under different flow rates of the forward channel. Different from the other three conditions, the intensity of pressure fluctuation under rated flow shows the least value. In addition to this, the symmetric results of four working conditions are presented due to the particular structure. The most serious fluctuation occurs in the small area that starts from the tongue, while the least severe fluctuation appears near the wall, far away from the tongue. Last but not least, it is noteworthy that the pressure intensity of all flow channels is quite low, except for the area near the tongue under the  $0.8 Q_d$ .



**Figure 10.** Pressure fluctuation intensity distribution on the mid-span of the forward channel under different flow rates.

Figure 11 shows the pressure fluctuation intensity distribution in the axial section under different flow rates of the volute. The value of the area, which includes the region near the volute tongue and the initial position of the first rib, descends as the flow rate ascends to the rated flow, which is attributed to the rotor-stator interaction as it gradually weakens. Furthermore, in Figure 11d, the value of the volute tongue and the initial position of the second rib begin to appear again (as shown in the red circle). Additionally, on the upper side of the diffusion section near the tongue, the flow streamline becomes more complex and affected by viscous wake structure. Compared with the low-pressure fluctuation intensity of the forward channel in Figure 11b, the same condition on the volute indicates that the flow of the pump is uniform and stable.



**Figure 11.** Pressure fluctuation intensity distribution on the mid-span of the volute under different flow rates.

#### 4.3. Internal Energy Loss and Flow Characteristics

According to the research of Kock and Herwig et al. [22,23], this section quantitatively reveals the energy loss in the model pump under the four typical working conditions based on the principle of entropy generation. For turbulence, the entropy yield mainly consists of two parts: one is caused by the time average velocity, which is called the direct dissipation term. The other part is caused by fluctuating velocity and is called the turbulent dissipation term [24].

The per-unit volume of total entropy production rate (EPR) is defined as follows:

$$\dot{S}''' = \dot{S}'''_D + \dot{S}'''_{D'} \quad (15)$$

The entropy production rate caused by time-averaged velocity and pulsating velocity is shown in the following equations:

$$\begin{aligned} \dot{S}'''_D = & \frac{2\mu}{T} \left[ \left( \frac{\partial \bar{u}}{\partial x} \right)^2 + \left( \frac{\partial \bar{v}}{\partial y} \right)^2 + \left( \frac{\partial \bar{w}}{\partial z} \right)^2 \right] + \\ & \frac{\mu}{T} \left[ \left( \frac{\partial \bar{v}}{\partial x} + \frac{\partial \bar{u}}{\partial y} \right)^2 + \left( \frac{\partial \bar{w}}{\partial x} + \frac{\partial \bar{u}}{\partial z} \right)^2 + \left( \frac{\partial \bar{v}}{\partial z} + \frac{\partial \bar{w}}{\partial y} \right)^2 \right] \end{aligned} \quad (16)$$

$$\begin{aligned} \dot{S}'''_{D'} = & \frac{2\mu_{eff}}{T} \left[ \left( \frac{\partial u'}{\partial x} \right)^2 + \left( \frac{\partial v'}{\partial y} \right)^2 + \left( \frac{\partial w'}{\partial z} \right)^2 \right] + \\ & \frac{\mu_{eff}}{T} \left[ \left( \frac{\partial v'}{\partial x} + \frac{\partial u'}{\partial y} \right)^2 + \left( \frac{\partial w'}{\partial x} + \frac{\partial u'}{\partial z} \right)^2 + \left( \frac{\partial v'}{\partial z} + \frac{\partial w'}{\partial y} \right)^2 \right] \end{aligned} \quad (17)$$

where  $\dot{S}'''_D$  represents the direct dissipative entropy yield and  $\dot{S}'''_{D'}$  represents the turbulent dissipation entropy yield;  $\bar{u}$ ,  $\bar{v}$  and  $\bar{w}$  are time-averaged velocities, m/s;  $u'$ ,  $v'$  and  $w'$  are

pulsating velocities, m/s.  $T$  is the temperature, K;  $\mu$  is the dynamic viscosity, and  $\text{N}\cdot\text{s}/\text{m}^2$ ;  $\mu_{eff}$  is the effective dynamic viscosity,  $\text{N}\cdot\text{s}/\text{m}^2$ .

However, due to the very obvious wall effect of entropy production, it is necessary to consider the entropy production near the wall, and its calculation formula is as follows:

$$S_W = \int_S \frac{\vec{\tau} \cdot \vec{v}}{T} dS \quad (18)$$

where  $\vec{\tau}$  is the wall shear stress, Pa;  $\vec{v}$  is the velocity vector at the center of the first layer of mesh in the boundary layer.

Therefore, by integrating  $\dot{S}_D'''$  and  $\dot{S}_{D'}'''$  and considering the wall entropy production, the total entropy production formula in the calculation domain is obtained.

$$S = S_{\bar{D}} + S_{D'} + S_W = \int_V \dot{S}_D''' dV + \int_V \dot{S}_{D'}''' dV + \int_S \frac{\vec{\tau} \cdot \vec{v}}{T} dS \quad (19)$$

Figure 12 shows the trends of entropy production which are divided into  $S$ ,  $S_D$  and  $S_W$  respectively. The entropy production in the main flow area rises rapidly while the wall entropy production climbs gradually as the flow rate increases. More precisely, the maximum value of total entropy production is 136.6 W/K at 1.2  $Q_d$ , and the minimum value is 74.1 W/K at 0.6  $Q_d$ . The wall entropy production ranges from 18% at 0.6  $Q_d$  to 30% at 1.2  $Q_d$ , which occupies a considerable share.

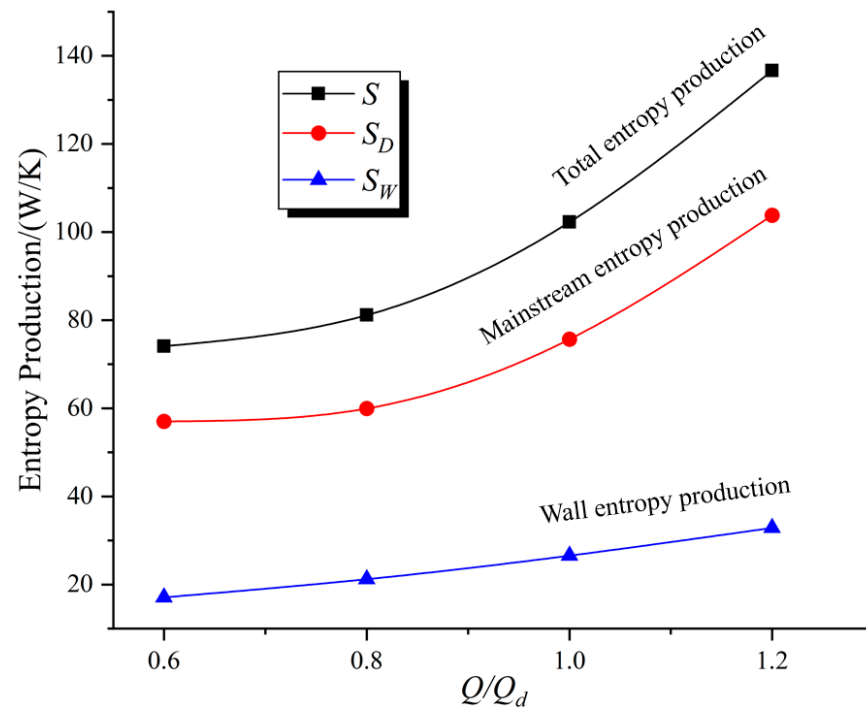
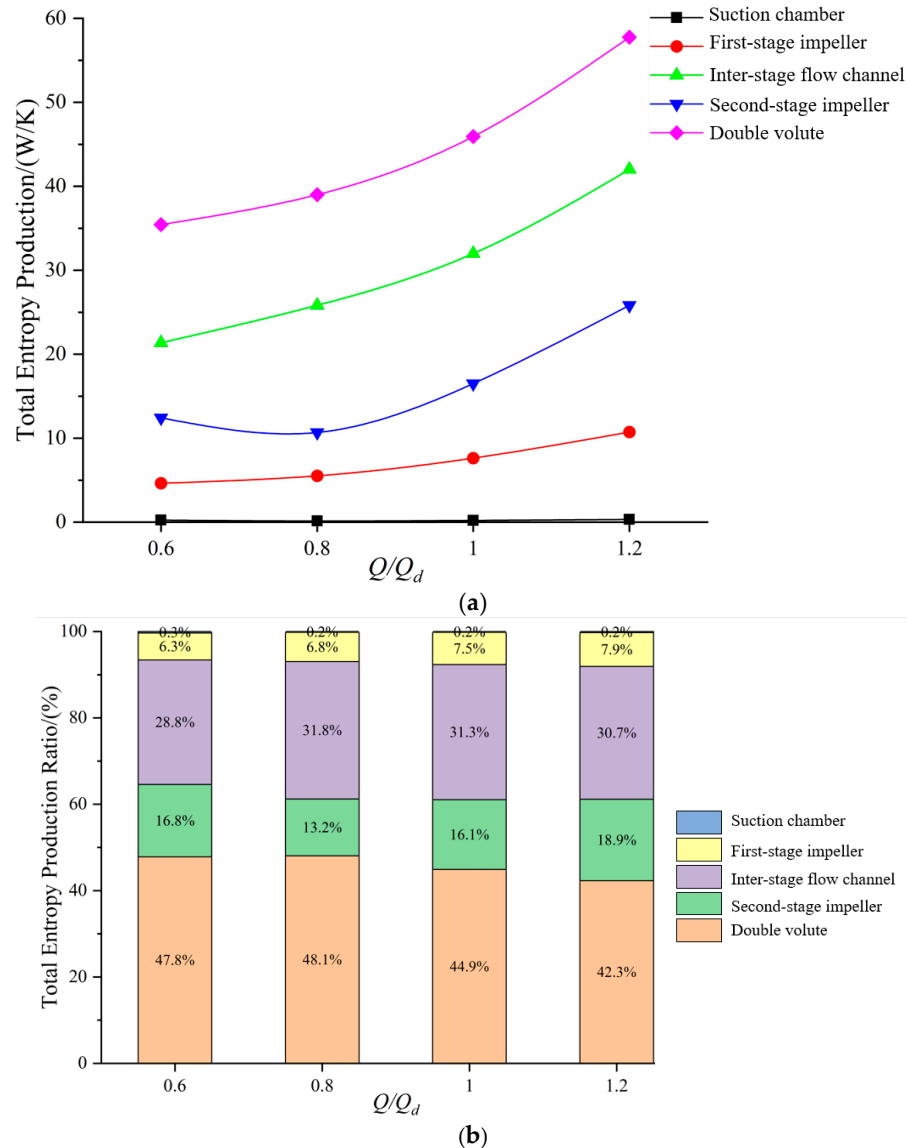


Figure 12. The trends of entropy production under different flow rates.

Figure 13 shows the total entropy production on different components of the pump and their corresponding proportions. The overall trend of total entropy production on four components is upward as the flow rate increases, except for the performance of the double-suction impeller, which falls at first and then goes up continuously. The total entropy production in the suction chamber is examined and shows a slight increase, which is usually considered constant. Additionally, the reason why the value on the inter-stage channel and double volute is larger than other components is that the energy loss among them is mainly in the form of impact loss and diffusion loss. From the perspective of

proportion, the corresponding total entropy generation ratio of each component is shown below under four different flow rates, which are sorted by descending order: double volute, inter-stage flow passage, second-stage impeller, first-stage impeller, and suction chamber. From the bar chart, it is obvious that the suction chamber is ignored in a small proportion. Additionally, the value of the double volute and inter-stage channel accounts for 70%, which is the key point of studying the entropy production.



**Figure 13.** Different representations of entropy production under different flow rates include (a) energy loss distribution and (b) total entropy production rate distribution.

## 5. Conclusions

The result of an unsteady simulation from the perspective of velocity field and pressure fluctuation using the detached eddy simulation was exhibited on the basis of a steady calculation. The high-speed zone occurs near the outlet of the suction chamber at different levels with a back-flow vortex when the pump runs. The existence of large-scale vortices and jet wakes is presented in the first-stage impeller, which seriously influences the efficiency of the pump. Besides, the flow regime of the inter-stage channel was deeply poor because of the structure, while the velocity trend in the second-stage impeller and double volute is relatively consistent under different conditions. The pressure fluctuation intensity of the

region near the impeller outlet and in the vicinity of the tongue generally increases, which is influenced by the rotor-stator interaction. Additionally, the phenomenon corresponded to the obvious gradient of velocity at the impeller outlet. The uneven structure mentioned above, combined with high pressure fluctuation intensity, brings about unnecessary energy loss, and the entropy generation ratio of the double-volute and inter-stage channel thus accounts for more than 70% of the total. Oppositely, the value of the suction chamber is ignored (under 1%). Overall, the outcome given by the detach eddy simulation can accurately and clearly show the internal flow of the pump.

For complex structure equipment, such as a multi-stage double-suction centrifugal pump, it is very complicated to generate the grid with high precision and carry out numerical simulation, especially with the RANS-LES turbulence model. Consequently, the article provides a scheme and resolution for solving the specific issue. Furthermore, the article adopts the mechanism of entropy generation to study energy loss, laying the theoretical groundwork for later design and optimization. Last but not least, the feature of pressure fluctuation in the multi-stage double-suction centrifugal pump is deeply discussed in the article, which is meaningful for the stable operation of this kind of pump.

**Author Contributions:** Conceptualization, J.P. and S.Y.; methodology, J.P.; software, J.P. and W.W.; validation, J.P., S.Y. and W.W.; formal analysis, J.P.; data curation, W.W.; writing—original draft preparation, W.P.; writing—review and editing, J.P., S.Y. and W.W.; funding acquisition, B.Z., J.W. and J.L.; resources, B. Z., J.W. and J.L. All authors have read and agreed to the published version of the manuscript.

**Funding:** The work was supported by the Open Research Subject of the Key Laboratory of Fluid and Power Machinery (Xihua University), Ministry of Education (szjj2019-007).

**Data Availability Statement:** Not applicable.

**Acknowledgments:** This work was supported by the Mount Taishan Industrial Leading Talent Project and Open Research Subject of the Key Laboratory of Fluid and Power Machinery (Xihua University), Ministry of Education (szjj2019-007).

**Conflicts of Interest:** The authors declare no conflict of interest.

## Nomenclature

Abbreviations	Description	Unit
$H$	Head	m
$nd$	Roatation speed	rpm
$Qd$	Design flow rate	$m^3 \cdot h^{-1}$
$P$	Static pressure	Pa
$\rho$	Water density	$kg \cdot m^{-3}$
$g$	Gravity acceleration factor	$m \cdot s^{-2}$
$t$	Time	s
$u$	Circumferential velocity	$m \cdot s^{-1}$
$\Psi$	Head coefficient	-
$\eta$	Efficiency	%
$\mu t$	Eddy viscosity coefficient	-
$v$	Relative velocity	$m \cdot s^{-1}$
$\bar{p}$	The time-averaged pressure component	pa
$\tilde{p}$	The periodic pressure component	pa
$C_p^*$	Pressure fluctuation intensity coefficient	-
$S$	Entropy production rate	$W \cdot K^{-1}$
$\dot{S}_D'''$	Entropy production rate caused by time-averaged velocity	$W \cdot m^{-3} \cdot K^{-1}$
$\dot{S}_D'''$	Entropy production rate caused by pulsating velocity	$W \cdot m^{-3} \cdot K^{-1}$
$T$	Temperature	K
$\mu$	Dynamic viscosity	$N \cdot s / m^2$
$\mu_{eff}$	Effective dynamic viscosity	$N \cdot s / m^2$

## References

1. Wei, Z.C.; Yang, W.; Xiao, R.F. Pressure Fluctuation and Flow Characteristics in a Two-Stage Double-Suction Centrifugal Pump. *Symmetry* **2019**, *11*, 65. [\[CrossRef\]](#)
2. Osman, M.; Wang, W.; Yuan, J.; Zhao, J.; Wang, Y.; Liu, J. Flow Loss Analysis of a Two-stage Axially Split Centrifugal Pump with Double Inlet under Different Channel Designs. *Proc. Inst. Mech. Eng. Part C-J. Mech. Eng. Sci.* **2019**, *233*, 5316–5328. [\[CrossRef\]](#)
3. Zhang, N.; Yang, M.; Gao, B. Investigation of rotor-stator interaction and flow unsteadiness in a low specific speed centrifugal pump. *J. Mech. Eng.* **2016**, *62*, 21–31. [\[CrossRef\]](#)
4. Xia, P.; Liu, S.; Wu, Y. Study on Flow Field of Impeller Tip Clearance in the Double Suction Pump. In Proceedings of the ASME 2005 Fluids Engineering Division Summer Meeting, Houston, TX, USA, 19–23 June 2005.
5. Chung, K.N.; Park, P.G.; Kim, J.Y. A Study in the Impeller-Volute Interactions of a Double-Suction Centrifugal Pump. In Proceedings of the Fluids Engineering Division Summer Meeting, Honolulu, HI, USA, 6–10 June 2003.
6. José, G. Unsteady Flow Patterns for a Double Suction Centrifugal Pump. *J. Fluids Eng.* **2009**, *131*, 071102.
7. Baun, D.O. *Hydrodynamic Forces in Centrifugal Pump and Compressor Impellers in Volute Casings: Measurements Using Magnetic Bearings and CFD Simulations*; University of Virginia: Charlottesville, VA, USA, 2002.
8. Barrio, R.; Parrondo, J.; Blanco, E. Numerical analysis of the unsteady flow in the near-tongue region in a volute-type centrifugal pump for different operating points. *Comput. Fluids* **2010**, *39*, 859–870. [\[CrossRef\]](#)
9. Choi, J.K.; McLaughlin, D.K.; Thompson, D.E. Experiments on the unsteady flow field and noise generation in a centrifugal pump impeller. *J. Sound Vib.* **2003**, *263*, 493–514. [\[CrossRef\]](#)
10. Kelder, J.; Dijkers, R.; Esch, B. Experimental and theoretical study of the flow in the volute of a low specific-speed pump. *Fluid Dyn. Res.* **2001**, *28*, 267–280. [\[CrossRef\]](#)
11. Slotnick, J.; Khodadoust, A.; Alonso, J. *CFD Vision 2030 Study: A Path to Revolutionary Computational Aerosciences*; National Aeronautics and Space Administration, Langley Research Center: Hampton, VA, USA, 2014.
12. Spalart, P. Comments on the feasibility of LES for wings, and on hybrid RANS/LES approach. *Adv. DNS/LES* **1997**, *1997*, 4–8.
13. Zhu, D.; Xiao, R.; Tao, R. Impact of guide vane opening angle on the flow stability in a pump-turbine in pump mode. *Proc. Inst. Mech. Eng. Part C J. Mech. Eng. Sci.* **2016**, *231*, 2484–2492. [\[CrossRef\]](#)
14. Minakov, A.; Sentyabov, A.; Platonov, D. Numerical modeling of flow in the Francis-99 turbine with Reynolds stress model and detached eddy simulation method. *J. Phys. Conf. Ser.* **2015**, *579*, 012004. [\[CrossRef\]](#)
15. Tao, R.; Xiao, R.; Liu, W. Investigation of the flow characteristics in a main nuclear power plant pump with eccentric impeller. *Nucl. Eng. Des.* **2018**, *327*, 70–81. [\[CrossRef\]](#)
16. Yang, J.; Xie, T.; Giorgio, P. Numerical study on rotating characteristics of unsteady flow inner pump-turbine in pump mode. *Int. J. Fluid Mach. Syst.* **2018**, *11*, 224–233. [\[CrossRef\]](#)
17. Wu, Y.; Liu, S.; Yuan, H. PIV measurement on internal instantaneous flows of a centrifugal pump. *Sci. China (Technol. Sci.)* **2011**, *54*, 270–276. [\[CrossRef\]](#)
18. Sun, H.; Xiao, R.; Wang, F. Analysis of the pump-turbine S characteristics using the detached eddy simulation method. *Chin. J. Mech. Eng.* **2014**, *28*, 115–122. [\[CrossRef\]](#)
19. Wang, Y.; Pei, J.; Yuan, S. Effect of Baffles in between Stages on Performance and Flow Characteristics of a Two-Stage Split Case Centrifugal Pump. In Proceedings of the ASME Fluids Engineering Division Summer Meeting, Waikoloa, HI, USA, 30 July–3 August 2017.
20. Strelets, M. Detached eddy simulation of massively separated flows. In Proceedings of the 39th Aerospace Sciences Meeting and Exhibit, Moffett Field, Reno, NV, USA, 8–11 January 2001.
21. Misra, A.; Pullin, D.I. A vortex-based subgrid stress model for large-eddy simulation. *Phys. Fluids* **1997**, *9*, 2443–2454. [\[CrossRef\]](#)
22. Kock, F.; Herwig, H. Local entropy production in turbulent shear flows: A high-Reynolds number model with wall functions. *Int. J. Heat Mass Transf.* **2004**, *47*, 2205–2215. [\[CrossRef\]](#)
23. Herwig, H.; Kock, F. Direct and indirect methods of calculating entropy generation rates in turbulent convective heat transfer problems. *Heat Mass Transf.* **2006**, *43*, 207–215. [\[CrossRef\]](#)
24. Zhao, J.; Pei, J.; Yuan, J.; Wang, W. Energy-saving oriented optimization design of the impeller and volute of a multi-stage double-suction centrifugal pump using artificial neural network. *Eng. Appl. Comput. Fluid Mech.* **2022**, *16*, 1974–2001. [\[CrossRef\]](#)

**Disclaimer/Publisher’s Note:** The statements, opinions and data contained in all publications are solely those of the individual author(s) and contributor(s) and not of MDPI and/or the editor(s). MDPI and/or the editor(s) disclaim responsibility for any injury to people or property resulting from any ideas, methods, instructions or products referred to in the content.